Characterization of a transition in the transport dynamics of a diffusive sandpile by means of recurrence quantification analysis

J. A. Mier,[1,*] R. Sánchez,[2] and D. E. Newman[3]
[1]*Departamento de Física Aplicada, Universidad de Cantabria, 39005 Santander, Spain*
[2]*Departamento de Física, Universidad Carlos III de Madrid, 28911 Leganés, Madrid, Spain*
[3]*Department of Physics, University of Alaska, Fairbanks, Alaska 99775-5920, USA*
(Received 31 May 2016; published 22 August 2016)

Recurrence quantification analysis (RQA) is used to characterize a dynamical transition that takes place in the diffusive sandpile. The transition happens when a combination of the drive strength, diffusivity, and overturning size exceeds a critical value. Above the transition, the self-similar transport dynamics associated to the classical (nondiffusive) sandpile is replaced by new transport dynamics dominated by near system-size, quasiperiodic avalanche events. The deterministic content of transport dynamics, as quantified by RQA, turns out to be quite different in both phases. The time series analyzed with RQA in this work correspond to local sand fluxes at different radial locations across the diffusive sandpile.

DOI: 10.1103/PhysRevE.94.022128

I. INTRODUCTION

The concept of self-organized criticality (SOC) [1] appeared over the latter half of the 20th century as a possible explanation for different observed dynamics of different physical and biological complex systems [2–6]. Their macroscopic behavior displayed the spatial and temporal scale invariance characteristic of the critical point of a phase transition, but without requiring any careful tuning of some parameter in order to reach the SOC state. SOC dynamics is often observed in slowly driven nonequilibrium systems, with a large number of elements entertaining nonlinear interactions. The key ingredient for the appearance of SOC is the existence of (a) an instability threshold and (b) two disparate time scales, one associated with the source of energy (or drive) and the other with the dissipation of energy (or relaxation). The main properties showed by systems in such a state are (1) spatial self-similarity (no characteristic lengths), (2) temporal persistence (memory effects), and (3) long-term (divergent) correlations. These properties are in contrast to those found in systems whose transport is dominated by pure diffusion, in which characteristic lengths (spatial locality) and time (lack of memory and uncorrelated dynamics) can be established.

In natural systems a competition between transport mechanisms with different dynamics is often observed. As an example, the transport of energy and particles in fusion plasmas magnetically confined in a tokamak can be considered, at least in certain regimes (see Ref. [7] for a thorough review), as the superposition of (at least) two different contributions: (1) an intermittent flux (referred to as the avalanche or SOC channel in what follows), driven by some kind of near-critical turbulence and (2) a continuous flux (referred to as the diffusive channel), driven by either collisions or some kind of supercritical turbulence. In cases like these, in which two (or more) channels contribute to transport, hybrid dynamical regimes should be expected in which the intrinsic nature of transport can itself change, in addition to the possible change in transport levels.

There is some experimental evidence pointing to the self-similar nature of plasma edge fluctuations and to the existence of avalanche-driven transport in real fusion plasmas in certain confinement regimes [7–10]. The SOC paradigm has been proposed as a relevant concept for the description of plasma transport in tokamaks [11,12]. It does indeed provide a framework in which some experimental findings [13–16], initially not understood, might find an explanation. The importance of the interaction between the SOC channel and standard diffusive channels in this context has been pointed out, in particular due to the enormous radial gradients present. In fact, it is the interest in understanding this interplay that first drove the efforts toward studying the dynamics of the diffusive sandpile [17]. In those studies, it was found that a remarkable transition took place that affected the global transport dynamics, as the relative importance of the diffusive channel increased sufficiently, even when it still remained strongly subdominant [18]. In particular, the transport dynamics changed abruptly, and the characteristic self-similar avalanche-like events typical of SOC systems were replaced by quasiperiodic constant-size edge-triggered events. As a result, the system lost most of its SOC properties.

In this article, we revisit this transition from the perspective offered by recurrence quantification analysis (RQA) techniques. This rather different take offers a complementary view to the referred previous studies that focused instead on estimators such as the sandpile profile roughness and avalanche statistics. The concept of recurrence, on which RQA is based, was first introduced by Poincaré while studying the three-body problem [19]. In that work, Poincaré claimed that, in volume-preserving flows with bounded orbits, the system recurs infinitely many times as close as one wishes to its initial state. Therefore, simply by following the evolution of state of any system, one could in principle search for recurrences in simulated (as is the case here) or experimental data. Then, associations could be drawn between the observed features of these recurrences and the underlying dynamics known to be active in the system. A powerful tool for the visualization and analysis of recurrences is the *recurrence plot* (RP), introduced by Eckmann *et al.* [20]. The methodology based on the analysis of recurrences in phase space using several

*mierja@unican.es

measures of complexity quantifying the small-scale structures in RPs is known as *recurrence quantification analysis* (RQA) [21].

The article is then organized as follows: in Sec. II the diffusive sandpile is introduced as a simple model that captures the basic physics of the interaction between SOC and diffusive transport channels. In Sec. III we describe the local flux time series from the diffusive sandpile that will be studied in the following sections. In Sec. IV we outline the basic concepts of recurrence plots and RQA. In Sec. V we apply RQA to the local flux time series before and above the dynamical transition takes place. In Sec. VI we interpret the RQA results in terms of the rules of the diffusive sandpile (that is, the physics of the problem!). Finally, Sec. VII contains our conclusions.

II. THE DIFFUSIVE SANDPILE MODEL

The running sandpile model has been extensively used to study the underlying physics aspects associated with the transport of particles in fusion plasmas [7,12,17,22]. The diffusive running sandpile is a driven directed running sandpile [23,24] with an additional diffusive component whose intensity can be tuned relative to the avalanche-like component. The sandpile domain consists of $L+1$ cells or sites, numbered from $x=0$ to $x=L$ (i.e., $x=0,1,\ldots,L-1,L$ are the allowed values). To each radial location x, a variable $h(x)$ is assigned that represents the amount of sand stored (or its height) in the cell at that site. The sandpile state evolves as follows: a grain of sand is dropped randomly on every cell at each iteration with probability P_0. The average external drive per cell and iteration is thus $S_0=P_0$. The SOC character of the sandpile dynamics arises from the existence of a critical slope Z_c that, when locally overcome, gives rise to the removal sand to the adjacent position. All cells are checked for stability at each iteration by comparing the local gradient $Z(x)=-[h(x+1)-h(x)]$ with the critical gradient $Z_c>0$. If $Z(x)>Z_c$,N_f grains of sand are moved to the next cell (see Fig. 1):

$$\begin{aligned} h(x) &= h(x)-N_f, \\ h(x+1) &= h(x+1)+N_f. \end{aligned} \tag{1}$$

In the diffusive sandpile, a second *diffusive* channel is added by establishing a local diffusive flux Γ_d at each cell given by $\Gamma_d(x)=D_0[Z(x-1)-Z(x)]=\Gamma_d^+(x)-\Gamma_d^-(x)$, where D_0 is the diffusion coefficient. The diffusive flux is simply the difference as the amount of sand reaching the cell at x due to diffusive transport from the cell at $x-1$ [$\Gamma_d^+(x)=D_0Z(x-1)$] minus the amount of sand leaving the cell at x due to diffusive transport to the cell at $x+1$ [$\Gamma_d^-(x)=D_0Z(x)$]. Naturally, the diffusive flux just described is equivalent to the application of the following rule at each step:

$$h(x)=h(x)+D_0[h(x+1)-2h(x)+h(x-1)], \tag{2}$$

a discrete version of a diffusive term like D_0d^2h/dx^2.

The rules of the sandpile are completed by imposing a closed boundary condition at $x=0$, so that no particle flux enters that cell from the left. The boundary condition applied at $x=L$ is open, so that all particles reaching the bottom edge of the sandpile are removed from the system.

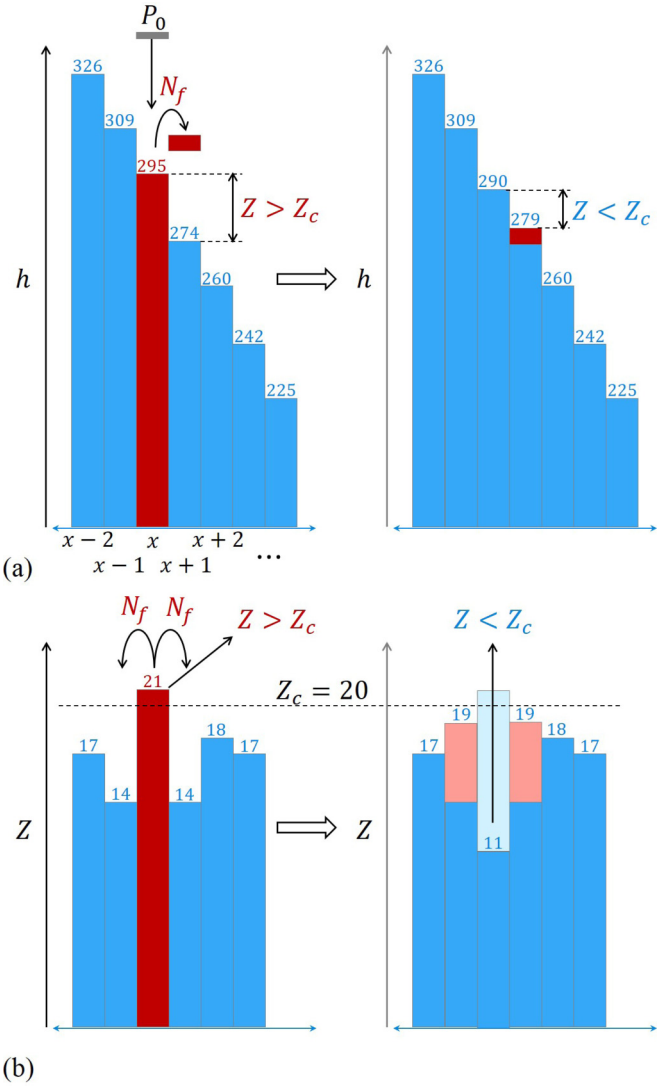

FIG. 1. (a) Sketch of the one-dimensional sandpile in real space explaining the corresponding automaton rules. (b) Sketch of the sandpile automaton rules in gradient space. The parameters for this sandpile are $Z_c=20$ and $N_f=5$. Red cells are unstable; the sand that has been moved to a location is shown in orange; the void left by the move, in light blue.

The diffusive running sandpile will reach a steady state under a continuous, fixed-average external drive. Assuming that the drive is spatially uniform, the sandpile domain will be split into two distinct subdomains once the steady state is reached. In the inner subdomain (extending outwards from $x=0$), transport of sand will be driven only by diffusion. In the outer subdomain (extending inwards from the boundary cell at $x=L$), transport will be driven by both diffusion and avalanches. Both subdomains match at a crossover point, whose mere existence establishes a limiting value of D_0 for avalanche-like transport to exist. Its location, x_t, is estimated by finding the largest position at which the integrated source in the range $[0,x_t]$ can be entirely evacuated by diffusion down the gradient while keeping the gradient below the average value at the SOC state that is given by $Z_a=Z_c-N_f/2$. (The estimation for Z_a is easy to do simply by inspecting Fig. 2.)

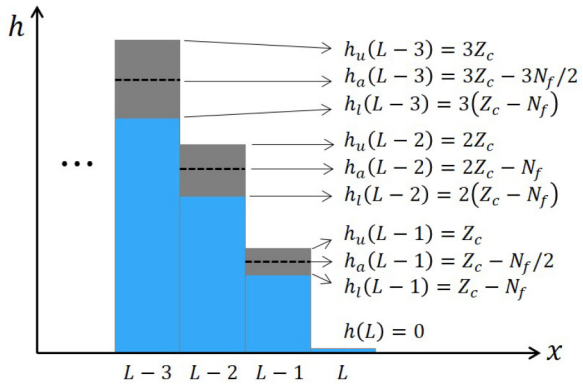

FIG. 2. Scheme with the possible values of h for the last four cells of the sandpile (case $D_0/P_0 = 0$). h_u,h_a, and h_l stand for the upper, average, and lower values of the height, respectively. $h(L) = 0$ is the boundary condition for the bottom cell. Since $h(L) = 0$, the upper limit on the height of the previous cell is $h_u(L-1) = Z_c$. Hence, $h(L-1) \leqslant h_u(L-1)$. But $h(L-1) \geqslant h_l(L-1) = Z_c - N_f$ to satisfy the steady state condition. Thus, its mean value is $h_a(L-1) = [h_u(L-1) + h_l(L-1)]/2 = Z_c - N_f/2$. The same principle can then be applied inwards.

The result is

$$\int_0^{x_t} S_0\, dx = P_0 x_t = \Gamma_d^-(x_t) = D_0 Z_a \rightarrow x_t = \frac{D_0 Z_a}{P_0}. \quad (3)$$

The analytical values for Z_a and x_t agree well with the simulations. The steady-state solutions for the sandpile profile on both subdomains can now be found to be, as long as $x_t < L$,

$$n(x) = Ax^2 + B, \quad 1 \leqslant x \leqslant x_t < L, \quad (4a)$$

$$n(x) = Z_a(L - x), \quad x_t \leqslant x \leqslant L, \quad (4b)$$

with

$$A = -\frac{P_0}{2D_0},$$

$$B = Z_a L - \frac{Z_a^2 D_0}{2P_0}. \quad (5)$$

The condition $x_t < L$ translates, in terms of the parameters of the simulation, into $D_0/P_0 < L/Z_a$, that sets an upper limit for the diffusivity ratio D_0/P_0. Otherwise the sandpile will exhibit the typical parabolic profile of diffusive systems, and SOC dynamics will be absent. The crossover point given by Eq. (3) moves outwards (inwards) for increasing (decreasing) diffusivity or decreasing (increasing) drive. Interestingly, the quantity $D_0 Z_a/P_0 L = x_t/L$ gives the fraction of the total average transport leaving the sandpile through the diffusive channel. Therefore, the average ratio of the intensities of both channels can be tuned by varying D_0/P_0, for fixed Z_a and L.

Another quantity of interest for the diffusive sandpile is the average (in time) local flux of sand. This flux must be understood as the sum of two contributions, $\Gamma(x) = \Gamma_t(x) + \Gamma_d(x)$, where Γ_t stands for the avalanche flux and Γ_d represents the diffusive flux. In steady state, the average local flux must equal the integral of the drive between [0,x] [In particular, $\Gamma(L) = P_0 L$.]. The avalanche part of the flux can be written in terms of the probability of a cell of being unstable, $P_1(x)$,

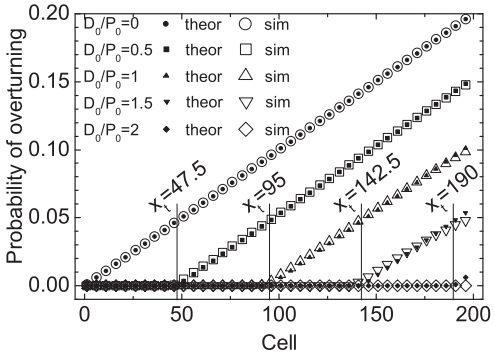

FIG. 3. Probability of overturning events per iteration as a function of the cell position for different values of the diffusivity ratio D_0/P_0. Filled symbols stand for the analytical estimation by means of Eq. (7). Open symbols stand for the simulations from the diffusive sandpile by using the following parameters: $L = 200, Z_c = 100, N_f = 10$, and $P_0 = 0.01$.

via

$$\Gamma_t(x) = P_1(x) N_f. \quad (6)$$

$1/P_1(x)$ also represents the number of iterations, on average, between two successive flips happening at the cell located at x, known as the average waiting time. $P_1(x)$ can be easily estimated to be

$$P_1(x) = 0, \quad x \leqslant x_t,$$

$$P_1(x) = \frac{P_0 x - D_0 Z_a}{N_f}, \quad x \geqslant x_t. \quad (7)$$

In fact, Eq. (7) permits us to estimate x_t as the radial position inside of which all cells are stable. Indeed, requiring $P_1(x_t) = 0$ in Eq. (7) yields the same value for x_t given by Eq. (3). Since transport is carried entirely by diffusion inside x_t,$\Gamma(x < x_t) = \Gamma_d(x) = P_0 x$ for $x < x_t$. For $x \geqslant x_t$, the diffusive flux stays roughly constant and at $\Gamma_d(x) \simeq D_0 Z_a$, since the average slope remains roughly constant at $Z_a = Z_c - N_f/2$ as we discussed previously. Therefore, the importance of the avalanche transport increases with x from x_t to L. This is illustrated in Fig. 3 that shows the probability of cell overturning, $P_1(x)$, as a function of x for increasing values of the diffusivity ratio D_0/P_0.

The diffusive sandpile just described was shown [18] to undergo a dynamical transition as the critical parameter $\kappa = (D_0/P_0)N_f^2$ was increased beyond a critical value $\kappa_c \simeq 22$. This parameter is related to the average variance of the slope across the avalanche region, or *roughness*, since it is proportional to the ratio of the expected roughnesses in the limits of $D_0 \rightarrow 0$ (pure SOC regime) and $D_0/P_0 > L/Z_a$ (pure diffusive regime since in that case $x_t = D_0 Z_a/P_0 > L$). The different dynamics governing transport above and below the transition are clearly illustrated in Fig. 4.

In the SOC-like regime (i.e., for $\kappa < \kappa_c$) transport takes place within the avalanche region in the form of avalanches (Fig. 4, left column) with a self-similar distribution of sizes, that can be initiated or stopped at any cell. Above the transition ($\kappa > \kappa_c$), however, transport becomes instead dominated by quasiperiodic avalanche events that are (almost always) initiated at the bottom edge of the pile and propagate

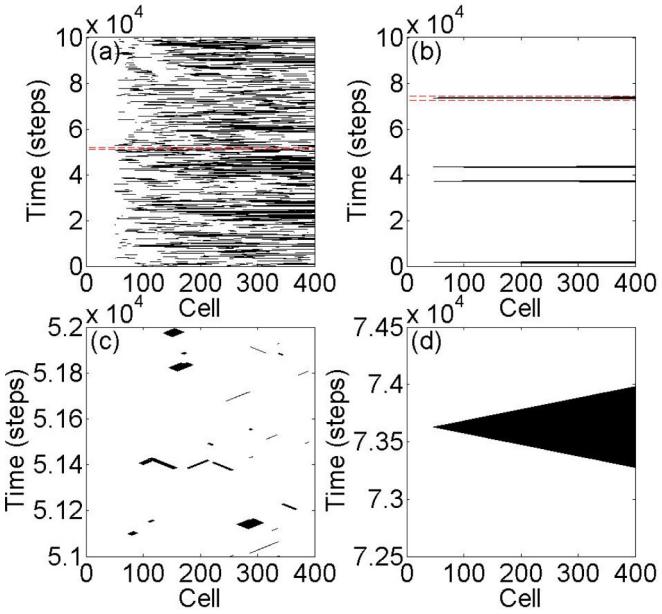

FIG. 4. Typical avalanche activity in the diffusive sandpile for parameter values that put its dynamics below (a–c) or above (b–d) the transition discussed in the main text. Unstable sites are represented with black dots and stable ones are represented with white dots (blanks). Panels (c)–(d) are zooms of the regions marked between horizontal, dashed lines in panels (a)–(b), respectively. Both simulations have identical parameters except that $N_f = 5 \rightarrow \kappa = 6.25$ in (a)−(c) and $N_f = 15 \rightarrow \kappa = 56.25$ in (b)−(d).

upwards to the crossover cell at x_t (which has been set to $\simeq 50$ for both simulations shown in Fig. 4). The temporal length (duration) of these quasiperiodic relaxation oscillations of constant amplitude in Figs. 4(b)–4(d) is found to be $D \simeq 2(L - x_t)$ ($\simeq 700$ steps in this case). The averaged waiting times associated to these relaxations after the transition can be easily estimated by imposing the balance between the temporal averaged incoming flux to the cell at $x = L$ (which in steady state is just the radially integrated source $S = P_0 L$) and the flux leaving that cell (sand leaving the pile) either through diffusive or avalanche-like transport channels,

$$P_0 L = D_0 Z_a + 2(L - x_t) N_f P_2, \tag{8}$$

P_2 being the probability associated to these edge-triggered, quasiperiodic avalanches of relatively constant amplitude. The corresponding averaged waiting times (w_t) will then be the inverse of this probability, $w_t = 1/P_2 \simeq 50\,000$ steps of the cellular automata, which agrees well with the numerical results of the automata. It is this change in dynamics that we will try to characterize in terms of the RQA techniques in the rest of the article.

III. FLUX TIME SERIES FROM THE DIFFUSIVE SANDPILE

Here we describe briefly the four types of sandpile time series ($\overline{\Gamma}_i$) to which RQA will be applied in the next sections. They all correspond to records of the local particle flux taken at some location within the diffusive sandpile (Γ), integrated

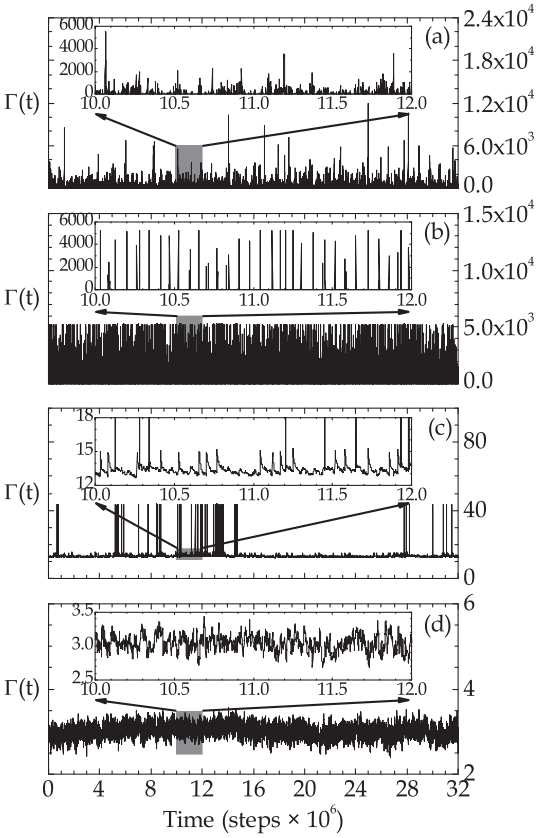

FIG. 5. Time records of $\Gamma(t)$ for different regimes: (a) below the transition, inside the SOC region ($x > x_t$); (b) above the transition, inside the SOC region ($x > x_t$); (c) in the vicinity of the crossover location ($x \simeq x_t$); and (d) within the diffusive region ($x < x_t$).

over a prescribed sampling period Δ; that is,

$$\overline{\Gamma}_i = \sum_{j=1}^{\Delta} \Gamma(\Delta[i-1] + j), \quad i = 1,2,\ldots,N, \tag{9}$$

where Γ in the summation represents the raw data coming from the sandpile simulations (see Fig. 5). Typically, $N = 32\,000$ in our simulations and $\Delta = 1000$.

Figure 5 shows four typical time flux signals obtained from the diffusive sandpile. The parameters used in our simulations are $L = 400, P_0 = 5 \times 10^{-4}, Z_c = 200$, and $N_f = 30$. For each signal in Fig. 5, an inset has been included that results from zooming out the shaded box in the main plot. The main difference between the four series is their location in the pile and the respective value of the so-called roughness parameter, $\kappa \equiv D_0 N_f^2 / P_0$. This parameter has been found to control the access to the dynamical transition in the diffusive sandpile [18], which happens if $\kappa > \kappa_c \simeq 22$.

The four signals picked for illustrating purposes are clearly quite different to the naked eye. In Fig. 5(a) the evolution of the particle flux at $x = 200$ is shown for a run with $D_0/P_0 = 1/900$ and $\kappa = 1 < \kappa_c$. The dynamics are purely SOC in this regime. That is, transport take place through avalanches over the SOC region; at any cell, local flux events exhibit power-law statistics and long-term memory. In contrast, Fig. 5(b) shows the temporal evolution of the particle

flux at $x = 200$ but for $D_0/P_0 = 140/900$ and $\kappa = 140 > \kappa_c$. Here transport becomes dominated instead by quasiperiodic relaxation oscillations that traverse the whole region; local flux events appear as quasiperiodic bursts of roughly constant amplitude. The reason for the change in dynamics through the transition is well understood [18]: the increased diffusion smooths out any irregularity of the sandpile profile caused by the falling rain so quickly that avalanches tend to originate at $x = L$, where the boundary condition forces the steepest slope, and propagate through the majority of the $x > x_t$ region scarcely encountering any obstacle. For the simulation used, $x_t \sim 30$. Hence, the $x = 200$ is well within the $x > x_t$ region. Next, Fig. 5(c) shows the evolution of the flux at the vicinity of x_t for the same simulation as Fig. 5(b). The inset shows some small quasiperiodic bursts, in addition to the usual large bursts associated to unstable cell overturnings. We will clarify their origin while trying to interpret the RQA results in later sections. Finally, Fig. 5(d) shows the time series of the flux for the same simulation but for cell $x = 6 < x_t$, within the diffusive region. This record resembles now a rather stochastic signal and is typical of diffusive-dominated transport.

IV. RECURRENCE QUANTIFICATION ANALYSIS OF THE DIFFUSIVE SANDPILE LOCAL FLUX TIME SERIES

Recurrences can be visualized and quantified by means of recurrence plots [21,25,26], which are graphical representations of symmetric matrices, whose elements can take only two values, namely, 0 or 1. These values codify instants in which two different states of the system are sufficiently close (1) or not (0) in phase space. RQA provides a great amount of information about the dynamics of any dynamical system through recurrence plots. It has been widely used in the study of nonlinear dynamics of complex systems and applied to areas as diverse as life science [27,28], earth science [29,30], astrophysics [31,32], chemical reactions [33], economical dynamics [34,35], and fusion plasmas [36–38].

In order to study recurrences, one starts by representing the states of the system as elements of a d-dimensional phase space, $\vec{y}(t) = \{y_1(t), y_2(t), \ldots, y_d(t)\}$, $\vec{y}(t)$ being vectors defining a trajectory in that phase space. However, not all the relevant components (d) are usually available to construct the corresponding state vector. Instead, we use some scalar time series of a representative quantity, $s_i = s(i\,\Delta t)$, where $i = 1, \ldots, N$, Δt being the inverse sampling frequency and N the number of temporal points. The phase space of the system can then be reconstructed by means of the time delay method:

$$\vec{s}_i = \{s_i, s_{i+\tau}, s_{i+2\tau}, \ldots, s_{i+(m-1)\tau}\}, \tag{10}$$

where m is the embedding dimension and τ is the time delay. The recursive plot is then constructed using the so-called recurrence matrix:

$$\mathbf{R}_{ij}(\varepsilon) = H(\varepsilon - \| \vec{s}_i - \vec{s}_j \|) \quad i, j = 1, \ldots, N. \tag{11}$$

Here $H(\cdot)$ is the Heaviside function, and the symbol $\| \cdot \|$ stands for a suitable norm. Therefore, $\mathbf{R}_{ij} = 1$, reflects the fact that states $\vec{s}_i$ and $\vec{s}_j$ visited by the system at times i and j were sufficiently close to each other, at least in the sense that $\| \vec{s}_i - \vec{s}_j \| < \varepsilon$, for some prescribed $\varepsilon > 0$. On the other hand, if $\| \vec{s}_i - \vec{s}_j \| > \varepsilon$, the corresponding entry in the matrix will be $\mathbf{R}_{ij} = 0$. The visualization of a recurrence plot is then performed by assigning different colors to the two values entries can take (see Fig. 6 for an illustration). Typically, black dots are assigned for recurrences and white dots for nonrecurrences.

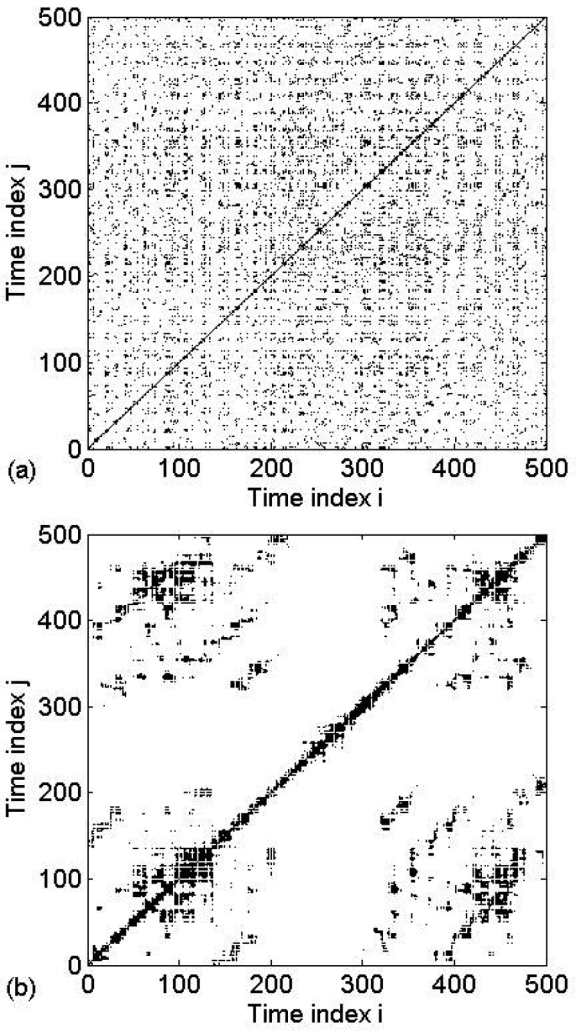

FIG. 6. Recurrence plots obtained from local fluxes at points where transport dynamics are different inside the diffusive sandpile: (a) within the diffusion-dominated region ($x < x_t$) and (b) within the avalanche region ($x > x_t$), but with transport dominated by large quasiperiodic avalanches ($\kappa > \kappa_c$). The parameters used are RR = 5%, $m = 4$, and $\tau = 20\Delta$.

The interpretation of recurrence plots then go as follows. Any black diagonal line in the recurrence plots represents a time interval over which the system state has followed a similar evolution as some other previous state; that is, $\vec{s}_i \approx \vec{s}_j$, $\vec{s}_{i+1} \approx \vec{s}_{j+1}, \ldots, \vec{s}_{i+l-1} \approx \vec{s}_{j+l-1}$, where l is the length of the diagonal line. On the other hand, vertical (horizontal) lines represent time intervals in which the system state has not changed much: $\vec{s}_i \approx \vec{s}_j$, $\vec{s}_i \approx \vec{s}_{j+1}, \ldots, \vec{s}_i \approx \vec{s}_{j+v-1}$, v being the length of the vertical (horizontal) line. The probability distribution of diagonal and vertical or horizontal lines in the recurrence plot offers a valuable tool to characterize the system nonlinear dynamics. Different estimators of complexity have been proposed [21] that attempt at quantifying the shape

and size of these structures, constituting the basis of the aforementioned recurrence quantification analysis (RQA). However, we will introduce only the two estimators that will be used in what follows.

The simplest RQA measure is the *recurrence rate* (RR), which quantifies the density of recurrence points in the recurrence plot. It is defined as the ratio of recurrence points to the total number of points. A second RQA measure deals with diagonal lines and is based on the histogram of diagonal lines of length l, $p(l)$. It is known as *determinism* (DET), being given by the ratio of recurrence points included in diagonal lines (of at least length $l_{\min}$) to all recurrence points:

$$\mathrm{DET} = \frac{\sum_{l_{\min}}^{l_{\max}} l p(l)}{\sum_{1}^{l_{\max}} l p(l)}. \tag{12}$$

For deterministic dynamics one expects that DET will be close to unity since any initial condition would follow the same evolution. On the other hand, for random dynamics, DET will be close to 0. It is important to choose a proper value for $l_{\min}$ in order to compute a meaningful DET. It should be sufficiently large as to exclude the kind of short diagonals formed by a mere tangential motion of the phase space trajectory [21]. On the other hand, if it is chosen too large, the lack of good statistics will render the value of DET meaningless.

V. RQA APPLICATION TO THE LOCAL FLUXES OF THE DIFFUSIVE SANDPILE

We proceed now to apply RQA to several time series of the local fluxes at different locations of the diffusive sandpile. Several technical details about the calculation of the recurrence plots are discussed first.

A. RQA general parameters

1. Recurrence rate and value of ε

All recurrence plots have been calculated while keeping the value of the RR fixed. That is, ε is calculated for each plot so that RR remains the same. In this way, we can draw meaningful comparison between recurrence plots for regimes with different dynamics. This is important for the sandpile when varying the diffusion parameter of the sandpile D_0/P_0. Specifically the value of the recurrence rate has been fixed to $\mathrm{RR} = 0.05$ (5%) throughout this article. Second, we have used the standard Euclidean L_2 norm to calculate distances between states.

2. Time delay

The accepted prescription is to set the value of the time delay τ to be set at least of the order of the temporal decorrelation time of the input signal [39,40]. The physical justification for this choice is that we are interested in the mesoscale dynamics, i.e., temporal scales well beyond the duration of any single avalanche. In the sandpile, avalanche durations are within the interval $[1, L]$. Thus, the decorrelation time of the temporal flux series, $\tau_d \sim L$, is much less than the inverse sampling frequency, $\Delta = 1000$. Therefore, in order to ensure that we are in the mesoscale, we have used $\tau = 20\Delta$ for all of the calculations. In addition, the portion of the time series considered to construct any recurrence plot has been chosen to be $25\tau = 500\Delta = 500\,000$ iterations long. This value is adequate over the range of values of D_0/P_0 used in the sandpile simulations examined here.

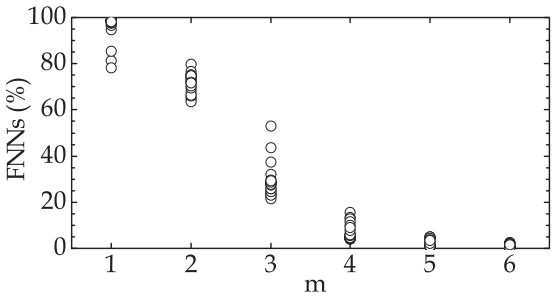

FIG. 7. Fraction of false nearest neighbors as a function of m for different values of the diffusion parameter D_0/P_0.

3. Embedding dimension value

Regarding the embedding dimension (m), we follow the accepted prescription of determining it using the False Nearest Neighbors (FNN) algorithm [41–43]. A sound election of m is important. If the value is too small, the geometry of the attractor cannot be unfolded in the reconstructed space. If m is too high, the diagnostics characterizing the dynamics can produce unreliable or spurious results [21]. The FNN algorithm is a powerful tool to estimate the correct number of time-delay coordinates. It consists in finding the nearest neighbor of each state vector with respect to some norm (the L_2 norm in our case). For any $m > 0$, let $\vec{s}_i = \{s_i, s_{i+\tau}, \ldots, s_{i+(m-1)\tau}\}$ be the state vector of the system at time i and let $\vec{s}_i^{\,n} = \{s_i^n, s_{i+\tau}^n, \ldots, s_{i+(m-1)\tau}^n\}$ be its nearest neighbor at the same time. We then compare the distance between them when increasing their dimension by 1, that is, adding $s_{i+m\tau}$ and $s_{i+m\tau}^n$ to each state vector. If $|s_{i+m\tau} - s_{i+m\tau}^n|$ is large compared to the new state distance $\|\vec{s}_i - \vec{s}_i^{\,n}\|$, the original states were close just because of the projection onto the embedding space and are classified as false nearest neighbors. On the other hand, if $|s_{i+m\tau} - s_{i+m\tau}^n|$ is small compared to $\|\vec{s}_i - \vec{s}_i^{\,n}\|$, they remain as near neighbors. Repeating this operation for all possible states, one can quantify the fraction of false nearest neighbors as a function of m. The suitable m value can then be determined as the one for which this fraction is sufficiently small. Here we have declared a neighbor false whenever the condition $|u_{i+m\tau} - u_{i+m\tau}^n| > 15\|\vec{u}_i - \vec{u}_i^{\,n}\|$. Figure 7 shows that a proper embedding is then obtained by choosing $m \geqslant 4$, which keeps the fraction of FNN below 10% on average. This result is rather insensitive to the value of D_0/P_0 used in the sandpile simulations.

B. RQA results

1. Recurrence plots for the diffusive sandpile

For illustrative purposes, Fig. 6 shows two typical recurrence plots obtained for local flux time series from the diffusive sandpile. Figure 6(a) is obtained from the local flux at a point within the diffusive region of the diffusive sandpile (i.e., $x < x_t$). It is representative of a case with a low degree of determinism, as can be easily assessed from its

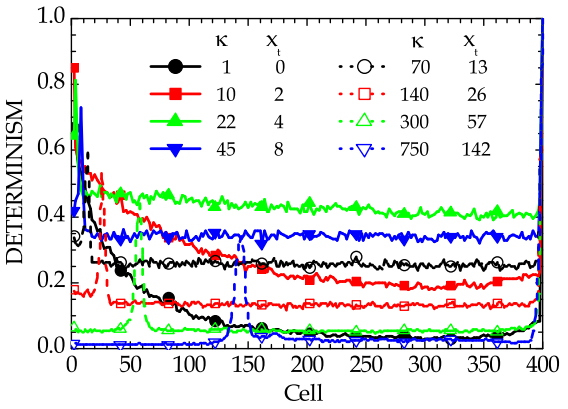

FIG. 8. Temporal averaged determinism of the flux temporal series as a function of the position for varying values of the parameter κ. The parameters used in the simulations were $L = 400, P_0 = 5 \times 10^{-4}$, $N_f = 30$, and $Z_c = 200$.

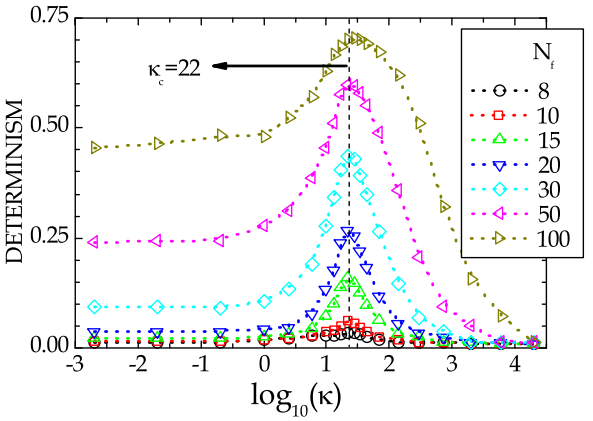

FIG. 9. Averaged determinism of the flux series as a function of $\log_{10}(\kappa)$ for several values of N_f.

visual inspection. It presents recurrent points that are isolated (except at the main diagonal, which simply states the perfect correspondence of a state with itself!), or in very small groups; the landscape is rather erratic. Figure 6(b), on the other hand, is obtained from the local flux at a point within the avalanche region (i.e., $x > x_t$) and above the dynamical transition (i.e., $\kappa > \kappa_c$). It illustrates a case with a higher level of determinism. Here recurrent points are grouped in clusters of different sizes, and there is an abundance of diagonal and vertical or horizontal structures.

2. *Determinism (DET)*

We have calculated recurrence plots, using the same parameters and procedure as used to produce those in Fig 6, for the local fluxes at many different positions of the diffusive sandpile, and for a wide range of values of the diffusion parameter D_0/P_0. Using Eq. (12) (and choosing a value $l_{\min} = 4$, that is sufficiently large to avoid tangential motion of trajectories in phase space while still including meaningful statistics), we have then quantified the degree of determinism DET as diffusion is varied. Since the local flux data available are much longer than the temporal window used for the recurrence plot calculation, results have been averaged over multiple temporal windows (64, in most cases) to reduce uncertainties. Figure 8 shows the radial dependence of the time-averaged DET at each sandpile cell for increasing values of the roughness parameter $\kappa = D_0 N_f^2 / P_0$.

The figure shows rather interesting features. First, it exhibits two strong peaks at the two edge positions of the avalanche region (i.e., $x_1 = x_t$ and $x_2 = L$), the former of which drifts towards larger x as D_0/P_0 is increased (as it should, since $x_t = D_0 Z_a / P_0$). The same behavior at the edge points is observed for every value of κ, either below or above the transition at κ_c. Secondly, two distinct behaviors are observed throughout the avalanche region depending on whether $\kappa < \kappa_c$ or $\kappa > \kappa_c$. Below the transition, DET decreases slowly from the peak value at x_1 as x is increased; in addition, the minimum value it reaches, before suddenly raising again as x approaches x_2, increases with κ. Indeed, that saturated DET is about 0.1 for $\kappa = 1, 0.2$ for $\kappa = 10$ and 0.4 for $\kappa = 22$. Things change quite dramatically above the transition, when $\kappa > \kappa_c$. In this case, the value of DET throughout the avalanche region is rather constant (except the two peak values at x_1 and x_2) and decreases instead as κ is increased above κ_c.

A more convenient way to characterize the dynamical transition using RQA is to look at the value of DET averaged over all sandpile cells. Figure 9 shows this value as a function of the logarithm of the roughness parameter, $\log_{10}(\kappa)$, for several values of N_f.

All curves exhibit a clear jump around $\kappa = \kappa_c \simeq 22$ (see vertical dashed line), which coincides very well with the critical threshold reported in Ref. [17]. All curves also show that, for values of κ well below κ_c, the DET value saturates at a final value that is an increasing function of N_f. As will be remembered, these cases correspond to parameter values in which the avalanche region transport is dominated by classical SOC-like behavior. On the other hand, the value of DET decreases towards zero for $\kappa \gg \kappa_c$, when the avalanche region transport is dominated instead by quasiperiodic relaxations and SOC dynamics disappear. The decrease happens, however, more slowly as N_f is larger.

VI. DISCUSSION OF THE RQA RESULTS

We proceed to discuss next the interpretation of the RQA results described in the previous section, relating them to the diffusive sandpile working rules. This exercise will provide some new insights about how the sandpile dynamics change in the presence of finite diffusion.

The first thing to bear in mind is what DET actually measures: the importance of (sufficiently long) diagonal lines in the recurrence plots. These lines are obtained by looking for similar local flux quartets $(\overline{\Gamma}_{i_1}, \overline{\Gamma}_{i_2}, \overline{\Gamma}_{i_3}, \overline{\Gamma}_{i_4})$, formed by the values of the local flux at four successive times separated by $\tau \sim 20\,000$ iterations, across the 500 000 iteration-long temporal window examined. The characteristic number of iterations that an avalanche needs to pass through any cell of the sandpile is of the order of the avalanche region, $L - x_t < L = 400$. Since the four members of the flux quartet are separated by many more iterations than L, a long diagonal line implies that there is some local process taking place that virtually repeats itself every time it happens, and that lasts for

periods of time much longer than single avalanches. From the behavior of the values of DET described previously, it is clear that these processes must be different in the diffusive part ($x < x_t$) and in the avalanche part ($x > x_t$) of the diffusive sandpile. Also, they change fundamentally over the avalanche region as D_0/P_0 is increased and the transition is crossed. The boundaries of the avalanche region, x_1 and x_2, also seem to have a behavior of their own. Why? and Which are these long-term processes that drive the large values of DET?

In what follows, we will argue that the physical mechanism behind these processes is related to how diffusion concomitantly erases the roughness of the profile across the avalanche region. This process should be uniform in space and should yield constant (on average) values of DET across the avalanche region, that should increase below the transition with D_0/P_0, and decrease afterwards. However, finite-size effects cause that the two boundaries, at x_t and L, behave rather differently to the other cells. The finite diffusion then transmits this odd behavior into the avalanche region, causing the spatial dependence in DET observed in Fig. 8, which is more acute below the transition. To base these claims, however, one needs to look in more detail at how avalanches happen in the sandpile.

A. Avalanches in the sandpile

The diffusive sandpile is simple enough that one can easily identify the main processes that take place in it. First, there is the random rain that drives the roughness of the sandpile profile; that is, the local variation of the slopes with respect their neighbors. Whenever a grain of sand falls at a cell, it instantly increases its height by $+1$, but it also increases the local slope by $+1$ and reduces the slope of the previous cell by -1. Since rain can fall randomly anywhere with the same probability, each local slope carries out a separate random walk, going up and down with equal chance. Whenever any local slope undergoing this process overcomes the local stability threshold, Z_c, an avalanche starts. The location of that starting point must correspond to a local *bump* in slope, that is, so close to the critical threshold Z_c that a single grain of sand added by the rain can make it topple. Figure 10 illustrates the process.

In red, we see a cell (No. 14) whose local slope exceeds the critical threshold after rain has dropped on it. The rules of the sandpile move N_f grains of sand to the next cell, which, in slope space, implies that their respective slopes are increased by $+N_f$ while the local slope at the originally unstable cell is reduced by $-2N_f$. The two neighbor cells (No. 13 and No. 15 in Fig. 10) are checked for stability next, and the process continues to propagate both upwards and downwards from the initial cell until a local *hole* in slope is encountered in each direction. By local *hole* we mean a cell whose local slope is sufficiently below the critical threshold that the addition of N_f is not enough to make it go unstable. In the case illustrated in the figure there is one such hole at cell No. 10 (above the initially unstable cell) and at cell No. 16 (below). The final result of the avalanche, as seen in the lower, right frame of Fig. 10, is that the local slope of all cells crossed by the avalanche remain in the same state as before, except for the initial bump that is now gone (the local slope at cell No. 14 has been reduced by $-N_f$), the two holes (above and below) that

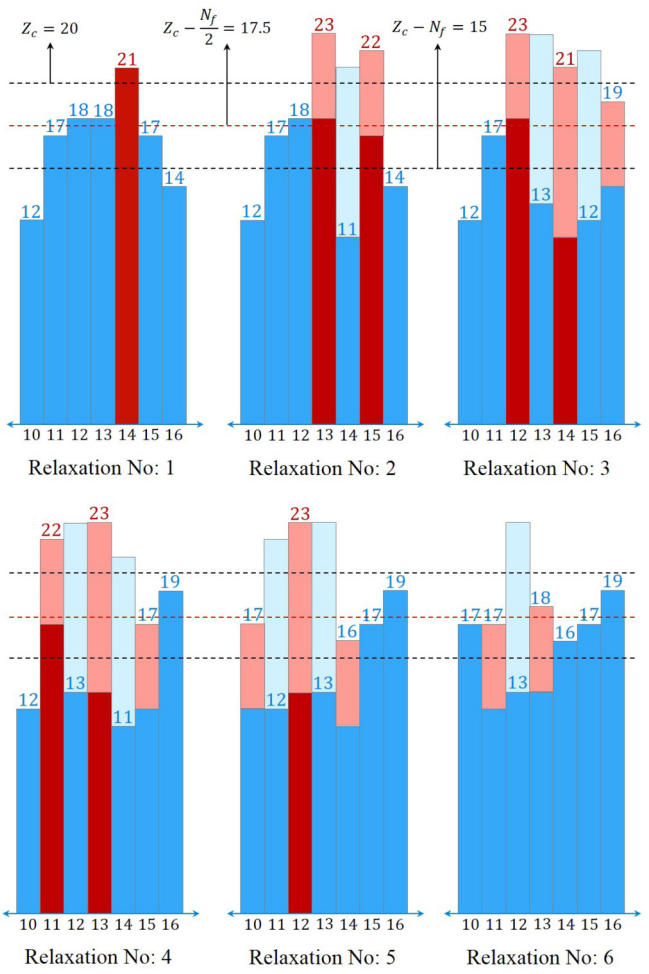

FIG. 10. Evolution of an avalanche in $|Z|$ space for a sandpile with $N_f = 5$ and $Z_c = 20$ (see text for explanation). Mean slope profile is around $Z_c - N_f/2 = 17.5$, as shown with a red dashed line.

are also gone (the local slope has been increased by $+N_f$), and a *new hole* that has appeared at the cell that is two positions below the upwards stopping point (cell No. 12 in this case). This is the way in which things happen across the avalanche region. Avalanches start at local bumps, stop at the closest hole locations (above and below), and produce a new hole above the original starting position that will act as a stopping point for future avalanches. Due to the slow rain rate, the influence of holes and bumps in the profile (that is, its roughness) is felt for very long periods of time, usually much longer than single avalanches as shown in many other works [12,24]. It is their presence and slow evolution that causes the large values of DET. It is also to be expected that DET should increase in the presence of diffusion, specially for small values that do not significantly modify the SOC dynamics that thrives on the avalanche mechanism just described, since the slow diffusive smoothing of the bump will delay local avalanche triggering leading to a longer, persistent, and more recognizable trace in the local flux signal. It should also increase with N_f, as shown in Fig. 9, since the larger N_f means deeper holes and higher bumps. However, the rain is dropped uniformly in space, and therefore, the distribution of holes and bumps should be pretty

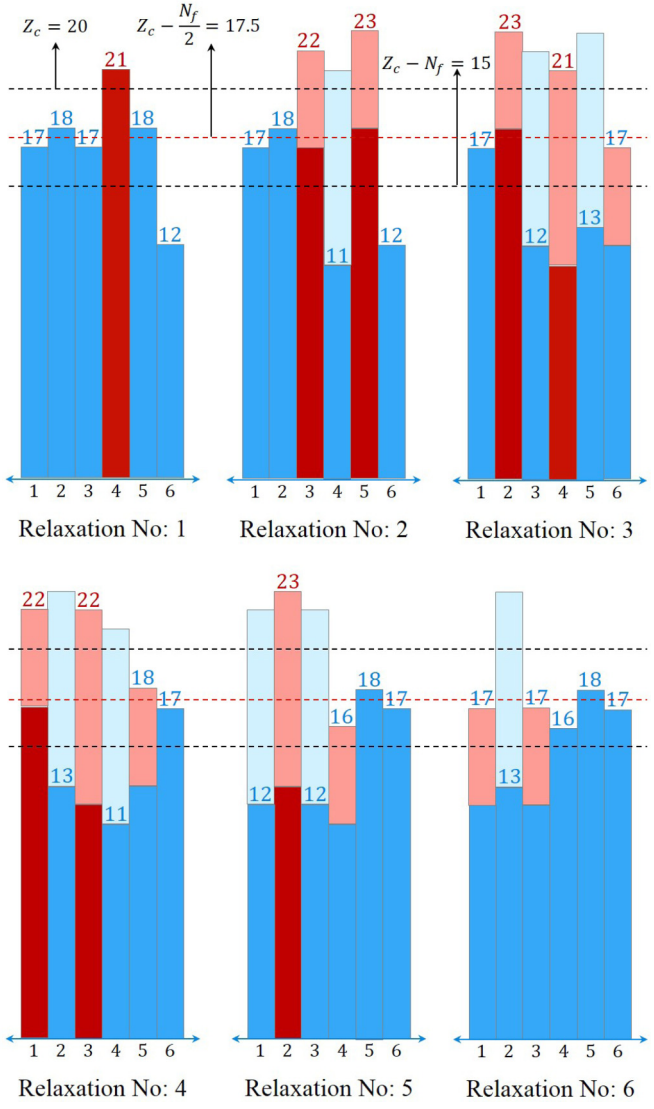

FIG. 11. Evolution of an avalanche that reaches the center of the pile in $|Z|$ space for a sandpile with the same parameters as in Fig. 10 (see text for explanation).

uniform all throughout the sandpile. As a result, we would expect the value of DET to be roughly constant across the avalanche region in the SOC regime. This is not what we found in the previous section though. Why?

B. Situation at the inner boundary, $x = x_t$

Things become a little bit different at the crossover point $x = x_t$ (also at the other boundary, $x = L$, which we discuss separately in the next subsection). To illustrate the situation, we focus first on the pure SOC sandpile, where $x_t = 0$. Figure 11 shows a sketch of an avalanche that starts at cell No. 4 (i.e., $x = 3$).

As expected, in the next iteration, its local slope decreases by $-2N_f$ and that of the cells immediately below and above it increases by $+N_f$. The avalanche propagates as in the case of Fig. 10 except for the fact that here no *hole* exists above 4 (there is a *hole* that stops the downward propagation at cell No. 6, though!). Therefore the avalanche propagates all the way up to the first cell. It cannot go any further up the slope though. By following the sequence sketched in Fig. 11 one can easily see the final result. All cells traversed by the avalanche end up with the same slope expected for the bump at which it was initiated (cell No. 4, whose slope is reduced by $-N_f$) that is now gone, the first hole down from that bump (cell No. 6, whose slope has increased by $+N_f$) that also disappears, and the first cell next to the center (cell No. 2, whose slope has been reduced by $-N_f$) where a new bump has appeared. In the absence of diffusion, the hole at the second cell is only filled by avalanches that propagate upwards from the outer cells. But whenever this happens, the next avalanche will not stop until it hits the center, and the hole will appear again at cell No. 2. As a result, the cell next to the center has a much larger probability of stopping avalanches than any other cell in the pile (this is not the same as saying that more avalanches will actually stop there than anywhere else in the pile, since that number will depend on how many avalanches actually propagate all the way to the center!). This is the reason why DET has such a peaked value close to $x = x_t$! If we now consider cases in which D_0/P_0 is finite, the behavior (i.e., a lower average slope) will extend for cells with $x > x_t$, because the local slope at the hole will be flattened by diffusion, the more the larger D_0/P_0 becomes. This is the reason for the nonuniform behavior shown in Fig. 8, for values of κ below the transition.

C. Situation at $x = L$

At the sandpile edge, on the other hand, sand is forced to leave the sandpile at every iteration, which leaves no hole or bump there. This is illustrated in Fig. 12, for the purely SOC sandpile. Here an avalanche starts at cell No. 396 and reaches the edge, since there are no holes below it (there is one above, though, at cell No. 394 that stops the upwards propagation of the avalanche). The chunks of sand moving down the pile reach the edge, where they are vacated from the sandpile. But this process causes no change in the slope at or near the edge, in contrast to what happened at the center of the pile.

In addition, the rain behaves differently at the edge as well, mainly because rain does not fall at the edge cell (or if it is does, it is instantaneously removed). This means that the slope at the edge, i.e., $Z(L-1)$, no longer carries out a random walk in slope space, but an steady increase at a rate P_0 since it increases by one when rain falls on the $L-1$ cell but does not ever decrease. As a result, the time the slope of the $L-1$ cell needs to overcome Z_c is much shorter than in any other location of the sandpile. Avalanches will start more frequently at the edge than at any other location. This is the reason why the value of DET is larger at the edge. Similarly to what happened at the center, a finite value of D_0/P_0 simply spreads this behavior inwards.

The arguments just laid out for the edge cell (and also for the crossover location, as we did in the previous subsection) are easily confirmed by looking at the distribution of starting and stopping points for avalanches. In Fig. 13 the histograms of starting and stopping points are shown for a diffusive sandpile with crossover point at $x_t \simeq 50$. The histogram of starting points, on the left, shows a pronounced peak at the edge (due to the higher average slope we predicted) and a depletion

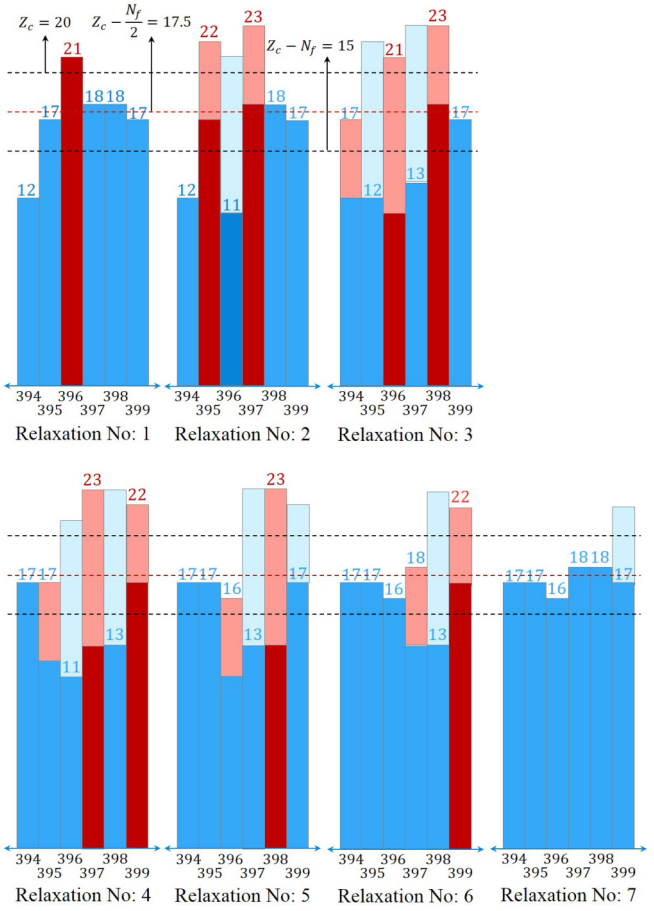

FIG. 12. Evolution of an avalanche that reaches the edge of the pile in $|Z|$ space for a sandpile with the same parameters as in Figs. 10 and 11 (see text for explanation).

as we approach the crossover point from $x > x_t$ (due to the lower average slope previously discussed). Everywhere else, the histogram is flat, as should be expected since avalanches are triggered by rain that is uniform in space. On the other hand, the histogram of stopping points, that should increase

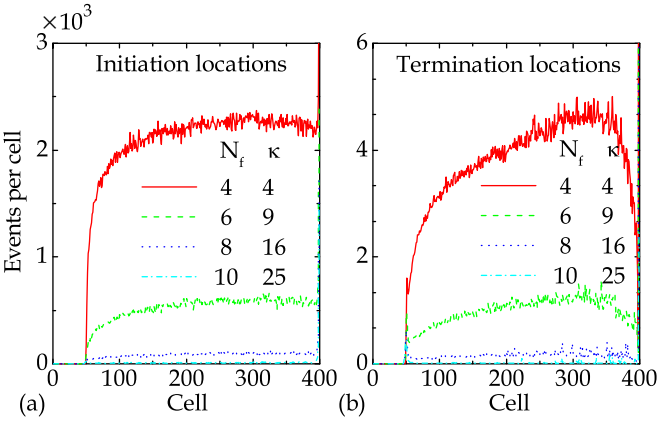

FIG. 13. Histogram of starting (left) and stopping (right) points for avalanches collected for several values of the parameter N_f. The parameters in common were $L = 400$, $D_0/P_0 = 0.25$, and $Z_c = 200$. Total duration of each run is 32×10^6 iterations.

linearly with x (since the amount of sand that needs to be transported down the slope must grow, as we move to larger x, to compensate the increased integrated drive over all previous cells), shows a clear peak at $x \sim x_t$ (due to the lower average slope previously mentioned) and at the edge. The edge peak is accompanied by a depletion of stopping points in cells close to the edge though. Both are a consequence of the larger average slope predicted at the edge, which diffuses inwards for finite D_0/P_0, which makes holes much more improbable in that region. This leads to a situation in which most avalanches that reach that region will make it out of the pile more often than not.

D. Behavior beyond the transition at $\kappa = \kappa_c$

The physical reason for the dynamical transition observed in the diffusive sandpile when $\kappa = \kappa_c$ has been attributed to diffusion becoming sufficiently large as to wipe out bumps and holes from the slope profile before they can act as starting or stopping points for avalanches [18]. It should be remarked that this can happen (and usually does) at values of D_0/P_0 sufficiently small as to maintain the sand being transported by the diffusive channel significantly below the avalanche channel. Since it is the presence of bumps and holes that caused the large values of DET observed below the transition, we expect them to decrease significantly for $\kappa > \kappa_c$. This is what Fig. 8 indeed shows. In addition, the singular behavior at x_t and L is still active above the transition, with significant larger values of DET close to them. But its influence can no longer propagate deep into the avalanche region, which results in a much more uniform value throughout the region. Finally, the value of DET for $\kappa \gg \kappa_c$ decreases more slowly with increasing N_f, as shown in Fig. 9, simply because holes are deeper and bumps higher for larger N_f. It simply takes more time to diffuse them away for the same D_0/P_0.

VII. CONCLUSIONS

In this work, we have characterized the dynamical transition that takes place in the diffusive running sandpile by using recurrence quantification analysis techniques. The RQA diagnostics have shown that the change in the dynamics of the sandpile, as the relative importance of the diffusive channel is increased, is correlated to a gradual change of the deterministic content of the local flux time series as measured at different locations of the sandpile. This change is due to the complex interplay between the continuous diffusive transport channel provided by $D_0 > 0$, and the avalanche transport channel, both of which are active over the avalanche region of the sandpile, and that changes significantly with the roughness parameter κ. Below the transition (i.e., when $\kappa < \kappa_c$), diffusion reinforces the deterministic character imprinted by avalanche propagation on the local fluxes. Above the transition ($\kappa > \kappa_c$), however, the effect is reversed and determinism, as measured by RQA, is continuously reduced. A last aspect revealed by the RQA analysis is that, although one would have in principle expected that the level of determinism be pretty uniform across the sandpile, finite-size effects are also important. They can affect the determinism value significantly, particularly at the two boundaries of the avalanche region,

being also able to penetrate quite deep into the avalanche region, particularly as the transition is approached from below ($\kappa < \kappa_c$).

ACKNOWLEDGMENTS

This research was sponsored by Ministerio de Economía y Competitividad of Spain under Projects No. ENE2012-31753 and ENE2012-33219. Research supported in part by DOE Office of Science Grant No. DE-FG02-04ER5741 at University of Alaska. Sandpile simulations have been run in *Uranus*, a supercomputer cluster located at Universidad Carlos III de Madrid (Spain) that has been funded by the Spanish Government via the national projects UNC313-4E-2361, ENE2009-12213-C03-03, ENE2012-33219, and ENE2012-31753.

[1] P. Bak, C. Tang, and K. Wiesenfeld, Phys. Rev. Lett. **59**, 381 (1987).
[2] B. E. Shaw, J. M. Carlson, and J. S. Langer, J. Geophys. Res. **97**, 479 (1992).
[3] P. Bak and K. Sneppen, Phys. Rev. Lett. **71**, 4083 (1993).
[4] B. Drossel and F. Schwabl, Phys. Rev. Lett. **69**, 1629 (1992).
[5] T. Nagatani, Physica A **218**, 145 (1995).
[6] S. Field, J. Witt, F. Nori, and X. Ling, Phys. Rev. Lett. **74**, 1206 (1995).
[7] R. Sanchez and D. E. Newman, Plasma Phys. Contr. Fus. **57**, 123002 (2015).
[8] B. A. Carreras, B. van Milligen, M. A. Pedrosa, R. Balbín, C. Hidalgo, D. E. Newman, E. Sánchez, M. Frances, I. García-Cortés, J. Bleuel, M. Endler, S. Davies, and G. F. Matthews, Phys. Rev. Lett. **80**, 4438 (1998).
[9] P. A. Politzer, Phys. Rev. Lett. **84**, 1192 (2000).
[10] G. Z. dos Santos Lima, K. C. Iarosz, A. M. Batista, I. L. Caldas, Z. O. Guimarães-Filho, R. L. Viana, S. R. Lopes, I. C. Nascimento, and Yu. K. Kuznetsov, Phys. Lett. A **376**, 753 (2012).
[11] P. H. Diamond and T. S. Hahm, Phys. Plasmas **2**, 3640 (1995).
[12] D. E. Newman, B. A. Carreras, P. H. Diamond, and T. S. Hahm, Phys. Plasmas **3**, 1858 (1996).
[13] N. Lopez Cardozo, Plasma Phys. Controlled Fusion **37**, 799 (1995).
[14] C. C. Petty *et al.*, Phys. Plasmas **2**, 2342 (1995).
[15] B. A. Carreras *et al.*, Phys. Plasmas **3**, 2903 (1996).
[16] A. Yoshizawa, S.-I. Itoh, K. Itoh, and N. Yokoi, Plasma Phys. Controlled Fusion **43**, R1 (2001).
[17] R. Sánchez, D. E. Newman, and B. A. Carreras, Nucl. Fusion **41**, 247 (2001).
[18] D. E. Newman, R. Sánchez, B. A. Carreras, and W. Ferenbaugh, Phys. Rev. Lett. **88**, 204304 (2002).
[19] H. Poincaré, Acta Math. **13**, 8 (1890).
[20] J. P. Eckmann, S. O. Kamphorst, and D. Ruelle, Europhys. Lett. **4**, 973 (1987).
[21] N. Marwan, M. C. Romano, M. Thiel, and J. Kurths, Phys. Rep. **438**, 237 (2007).
[22] R. Sánchez, D. E. Newman, B. A. Carreras, R. Woodard, W. Ferenbaugh, and H. R. Hicks, Nucl. Fusion **43**, 1031 (2003).
[23] L. P. Kadanoff, S. R. Nagel, L. Wu, and S.-M. Zhou, Phys. Rev. A **39**, 6524 (1989).
[24] T. Hwa and M. Kardar, Phys. Rev. A **45**, 7002 (1992).
[25] M. C. Casdagli, Physica D **108**, 12 (1997).
[26] M. Thiel, M. C. Romano, and J. Kurths, Phys. Lett. A **330**, 343 (2004).
[27] J. Zbilut, A. Giuliani, C. L. Webber Jr., and A. Colosimo, Protein Eng. **11**, 87 (1998).
[28] A. Giuliani, P. Sirabella, R. Benigni, and A. Colosimo, Protein Eng. **13**, 671 (2000).
[29] N. Marwan, M. Thiel, and N. R. Nowaczyk, Nonlinear Processes Geophys. **9**, 325 (2002).
[30] T. K. March, S. C. Chapman, and R. O. Dendy, Physica D **200**, 171 (2005).
[31] N. Asghari *et al.*, Astron. Astrophys. **426**, 353 (2004).
[32] O. Kopáček, V. Karas, J. Kovář, and Z. Stuchlík, Astrophys. J. **722**, 1240 (2010).
[33] M. Masia, S. Bastianoni, and M. Rustici, Phys. Chem. Chem. Phys. **3**, 5516 (2001).
[34] W. S. Chen, Physica A **390**, 1332 (2011).
[35] J. A. Bastos and J. Caiado, Physica A **390**, 1315 (2011).
[36] Z. O. Guimarães-Filho, I. L. Caldas, R. L. Viana, J. Kurths, I. C. Nascimento, and Yu. K. Kuznetsov, Phys. Lett. A **372**, 1088 (2008).
[37] Z. O. Guimarães-Filho, I. L. Caldas, R. L. Viana, I. C. Nascimento, Yu. K. Kuznetsov, and J. Kurths, Phys. Plasmas **17**, 012303 (2010).
[38] J. A. Mier, R. Sánchez, L. García, J. Varela, and D. E. Newman, Phys. Plasmas **18**, 062306 (2011).
[39] H. Kantz and T. Schreiber, *Nonlinear Time Series Analysis* (Cambridge University Press, Cambridge, 1997).
[40] L. Cao, Physica D **110**, 43 (1997).
[41] M. B. Kennel, R. Brown, and H. D. I. Abarbanel, Phys. Rev. A **45**, 3403 (1992).
[42] H. D. I. Abarbanel, R. Brown, J. J. Sidorowich, and L. S. Tsimring, Rev. Mod. Phys. **65**, 1331 (1993).
[43] H. D. I. Abarbanel and M. B. Kennel, Phys. Rev. E **47**, 3057 (1993).